

# Advanced fault location scheme for superconducting cables based on deep learning algorithms

Eleni Tsotsopoulou<sup>a,\*</sup>, Xenofon Karagiannis<sup>b</sup>, Theofilos Papadopoulos<sup>b</sup>, Andreas Chrysochos<sup>c</sup>, Adam Dyśko<sup>a</sup>, Qiteng Hong<sup>a</sup>, Dimitrios Tzelepis<sup>a</sup>

<sup>a</sup> Department of Electronic and Electrical Engineering, University of Strathclyde, Glasgow, G1 1XQ, UK

<sup>b</sup> Department of Electrical and Computer Engineering, Democritus University of Thrace, Xanthi, Greece

<sup>c</sup> R&D Department of Hellenic Cables, Athens, 15125, Greece

## ARTICLE INFO

### Keywords:

Convolutional Neural Network  
Fault location  
Image analysis  
Superconducting cable

## ABSTRACT

This paper addresses the challenge of fault localization in power grids which incorporate Superconducting Cables (SCs) and presence of inverter-connected generation, by proposing a novel data-driven fault location scheme. The developed fault location algorithm utilizes the transformation of time domain fault current and voltage signatures, to time–frequency domain and exploits the advantages of a Convolutional Neural Network (CNN) to estimate the fault position along SCs. The proposed algorithm has been tested using a verified model of SC, and the results revealed that it can provide precise fault localization for a wide range of fault scenarios, including different fault types, fault resistance values and fault inception angles. Furthermore, the proposed scheme robustness has been verified against different influencing factors accounting for very small increments of fault location, additive noise and different value of sampling frequency. For validation purposes, the effectiveness of the CNN-based algorithm has been compared with other data-driven algorithms and the relevant advantages have been highlighted.

## 1. Introduction

Power systems are experiencing a rapid transition, emanating from the gradual decommission of large Synchronous Generators (SGs) and the progressive deployment of Converter Interfaced Generation (CIG). The intermittent nature of the CIGs in conjunction with the immense increase in global electricity demand, have created reliability and resilience challenges to the future power grids. Consequently, there is a growing need for bulk power corridors to provide continent-wide sharing of electric power in an efficient way [1].

Superconducting Cables (SCs) are becoming increasingly competitive compared to conventional transmission lines and cables, by the virtue of superior advantages, such as their capability to transfer power over long distances at lower voltage levels and with reduced power losses [2]. Therefore, large-scale applications of SCs have been the focus of enormous research due to their unique physical characteristics [3].

The performance of SCs, during the steady-state and the transient conditions (i.e., faults), is dominated by the electro-magneto-thermal properties of the High Temperature Superconducting (HTS) tapes and the operating conditions of the system [4]. Subsequently, the installation of SCs, results in variations in the network performance (i.e., variable resistance, limited fault currents, etc.), emanating mainly from the

quenching of the HTS tapes. This has raised major fault management challenges accounting for detection, location and protection operation, which remain to be further investigated and resolved [5].

In transmission systems, when a fault occurs on a feeder, protection systems initiate the selective tripping of the corresponding circuit-breakers in order to prevent the adverse effects on the power system's operation. Following the fault detection, the precise estimation of fault location is of paramount importance in order to enable the rapid restoration of the system and minimize the down time [6]. Particularly, for the case of SCs the precise identification of fault location is very important considering their complex configuration (i.e., cooling liquid tubes, tapes, etc.) and the lack of standardization in the repair procedure.

In recent years, a variety of fault location methods have been reported in the literature, proposing different approaches such as impedance-based methods [7,8], travelling wave (TW) techniques [9, 10], time–frequency domain reflectometry [11,12], state estimation [13] and sparse measurements techniques [14,15]. Even though they all have their own advantageous features, their applicability is limited when it comes to SC due to their unique electro-magneto-thermal

\* Corresponding author.

E-mail address: [eleni.tsotsopoulou.2018@uni.strath.ac.uk](mailto:eleni.tsotsopoulou.2018@uni.strath.ac.uk) (E. Tsotsopoulou).

properties. For example, impedance-based methods are not suitable due to the dynamically changing impedance of SCs during faults which can lead to inaccurate fault location estimation. TW-based methods have been proven to provide accurate estimation of the fault position along the transmission lines by identifying the TW reflections and the time required for the wave to travel to the measuring point [16,17]. However, their implementation is accompanied by the installation of specialized and costly equipment (i.e., sensors, GPS etc.). Time-frequency domain reflectometry has been reported in the literature for the real-time abnormality diagnosis (i.e. fault detection and fault location) of SCs [18]. However, the proposed scheme requires the addition of measuring components necessary to measure independently the reflected signals generated by each phase, resulting in higher cost. Furthermore, validation studies do not consider the dynamically changing impedance of the layers of SC during quenching. Additionally, authors in [19] propose a Stepped Frequency Wave Reflectometry (SFWR) method for the identification of the fault location in joints, dielectric and other SC parts. The cable under-test is a single-phase 22.9 kV/50 MVA SC with length of 7 m. The resulting fault location estimation error is approximately 4.55%, while the proposed method has not been scrutinized against a variety of fault conditions, accounting for different fault types, locations or highly resistive faults. The same authors investigate the challenge of the fault localization on SCs in [20], by applying a fundamental Time-Frequency Domain Reflectometry (TFDR) approach on a similar prototype SC with length of 7 m. The accuracy of the fault location identification is increased, however, the fault location estimation error is affected by the SC temperature and the performance of the developed method has not been confirmed for a wide range of fault scenarios. An improved TFDR method incorporated with filter-Ensemble Empirical Mode Decomposition (EEMD) noise reduction is presented in [21] for a 50 m three-phase SC. The obtained fault location estimation error is approximately 0.01%. Nevertheless, the conducted work considered only the case of a solid three-phase fault. Therefore, it is evident that the technical literature is limited on the reflectometry-based approaches for the fault localization on SCs and the proposed methods have not been validated for multiple fault conditions (i.e., various fault locations along SC length, highly resistive faults), SCs with longer length and other factors which affect the accurate estimation of the fault position such as the noisy measurements. Furthermore, the need for external equipment and high sampling rates can be taken as drawback of these methods. Additionally, there are reported studies which investigate the impact of the Superconducting Fault Current Limiters (SFCLs) on the performance of the fault location schemes [22]. However, the influence of SFCLs on the power systems fault localization problem is out of scope of the presented work.

The increasing penetration of CIG-based technology has created the necessity for continuous network monitoring and installation of sophisticated metering equipment. On that front extensive research has started to be pursued regarding sparse measurements-based fault location schemes. Such techniques are based on the comparative analysis between actual voltage measurements acquired from multiple points along the network and simulated voltage signals for all potential fault cases. The fault location is estimated according to the optimal match between the two voltage signals. The influence of the monitoring devices distribution on the fault location accuracy is the major challenge of these methods. Insufficient and low cost devices leads to a compromise of fault location scheme accuracy and applicability. Furthermore, the development of synchro-phasor-based state estimation technologies could be a promising scheme for fault location application if the high cost of the required hardware is overcome.

To mitigate relevant challenges emanating from changes in power grids, accounting for the physical infrastructure and information layer, more advanced approaches have been emerged, based on data-driven Artificial Intelligence (AI) techniques. The potentials of AI-based schemes for fault diagnosis applications have gained popularity in the energy sector due to their capability to expose quantities which are

invisible in direct measurements and extract hidden patterns from the available data. Relevant deployment of AI technology for fault location applications include the utilization of Convolutional Neural Networks (CNNs) [23], Long Short-Term Memory (LSTM) [24], Support Vector Machines [25] and XGBOOST regressors [26]. Furthermore, by taking advantage of the tangible benefits provided by the AI techniques, many hybrid fault location schemes have been proposed in the technical literature which are based on the combination between feature extraction techniques, such as Wavelet Transform, and AI algorithms [27] or the enhancement of conventional methods performance with pattern recognition techniques [28]. Based on the literature review all the AI-based fault location methods provide high fault location accuracy and are robust against a variety of fault conditions. However, most of the reported methods have been evaluated based only on the testing dataset and do not consider previously unseen scenarios out of the initial dataset. Furthermore, no none of the proposed schemes has been scrutinized against small increments of fault location in order to validate the discrimination capability of the AI algorithms. Additionally, to the authors best knowledge despite the abundance of the proposed fault location schemes in the literature, there is no reported research which copes with the fault localization on SCs [29].

One major issue of the AI fault location schemes is the data availability and the computational requirements. As future power systems become data-rich, the emergence of Wide Area Measurement systems (WAMs) based on PMUs allows the access to plentiful data, accelerating the widespread adoption of data-driven applications. In regards to the computational requirements, as the technology advances the computational burden is progressively minimized. Therefore, the adoption of the AI-based methods in fault management applications presents unique advantages which outweigh the aforementioned challenges.

Driven by the recent advancements in AI and the emerging integration of SCs in modern power grids, the presented research builds upon the work conducted in [5] and addresses the challenges related to fault location on SCs integrated within a system with penetration of CIGs. For this purpose, authors developed a data-driven algorithm which forms the fault location estimation on SCs to a regression problem, utilizing image analysis techniques. The selection of the data-driven method is based on the aforementioned limitations of the conventional schemes and the ability of such techniques to acquire a deeper understanding of complex system topologies such as those which incorporate SCs. The proposed scheme relies on the three-phase current and voltage measurements only from one terminal of the SC and does not require the installation of any additional equipment. The developed algorithm combines the transformation of time domain signals to time-to-frequency domain (spectrograms) with Deep Learning (DL) algorithm (i.e., CNNs) in order to perform the image analysis for the fault location estimation. Even though image analysis has a plethora of interesting features for power systems applications and is considered an important field of the AI, there is a very limited number of publications for fault location problems [30]. Image analysis techniques are utilized to extract crucial features related to the power systems conditions based on historical data, removing the need for complicated and expensive phasor synchronous measurements equipment.

The optimal parameters of the developed algorithm have been selected by utilizing the grid-search technique in order to reduce the computational burden and improve the predictive capability of the fault location scheme. Furthermore, for the training process the K-fold validation technique has been adopted in order to eliminate the dependence of the algorithm in the training dataset and increase the generalization capability. The effectiveness of the proposed scheme has been assessed and validated under a wide range of scenarios including different fault types, fault resistance values and fault inception angles at various positions across the SC length. The high fault location accuracy of the developed method has been confirmed under extreme fault cases which considered high fault resistances, small fault locations increments and the addition of noise in the original dataset.

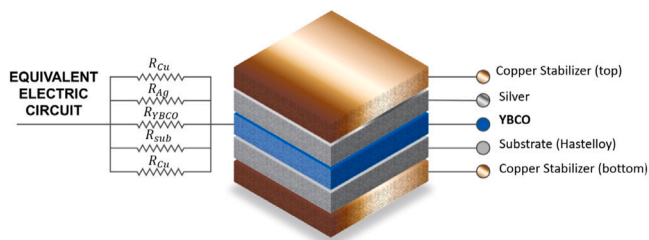


Fig. 1. Simplified structure of HTS tape.

The generalization capability of the proposed method has been further highlighted by considering image perturbation techniques during the training process. Additionally, its superiority has been verified by the comparison with other widely-used data-driven algorithms reported in the literature.

The main contributions of the proposed work can be outlined as follows:

- Development of a novel data-driven fault location scheme which addresses the challenge of the fault localization on SCs, by presenting increased generalization capability and higher fault location estimation accuracy compared to other data-driven algorithms. Furthermore, the proposed scheme presents enhanced scalability and deployability due to the eliminated need for synchronized measurements.
- Accurate fault localization on SCs, unaffected by the quenching phenomenon (i.e., variable resistance). Conversely to the existing fault location methods for SCs the developed scheme has been verified against various fault conditions, considering highly resistive faults, very small increments of fault location and noisy data.

## 2. Numerical modelling of SC

This section presents the modelling of the SC, which starts from the design of the HTS tapes and builds up to the three-phase cable. The SC was modelled in Matlab/Simulink, considering the electro-thermal properties of the HTS tapes in order to provide a realistic representation of the quenching during the transient conditions. It must be noted that the adopted modelling process constitutes an improvement of the procedure reported in [5].

### 2.1. Numerical modelling of HTS tapes

The electro-magneto-thermal properties of the HTS tapes, which are constructed as coated conductors, dominantly determine the characteristics of the SCs [4]. The main factors which affect the electro-magneto-thermal features of the HTS tapes include the three critical margins accounting for the critical current,  $I_{Cr}$ , the critical temperature,  $T_{Cr}$ , and the working magnetic field,  $B$ . A simplified structure of a commercially available second generation (2G) HTS tape has been modelled in the presented research according to [5,31] specifications. The employed tapes are discretized into different layers accounting for a superconducting layer, which is made of Yttrium Barium Copper Oxide (YBCO), two stabilizer layers made of copper, one substrate layer and one silver layer. The electric equivalent of one HTS tape is depicted in Fig. 1 and consists of parallel-connected resistances corresponding to each layer.

The core of the SC consists of the former which is modelled as a stainless steel tube [4] and acts as an alternative current path, along with the copper stabilizer layers during the quenching. Specifically, copper stabilizer layers and the former are ultimately utilized as means to protect the cable from excessive thermal stresses leading to its destruction. Under the normal operating conditions, the resistivity of the

YBCO layer is negligible and consequently current flows predominantly through this layer. However, during the transient conditions, once the current flowing through the HTS tapes, reaches values higher than the  $I_{Cr}$  and the quenching starts, the resistivity of the YBCO layer presents a dramatic increase which results in a subsequent increase in the temperature,  $T$ , of the SC. The HTS tapes start to lose their superconducting properties. If the generated Joule heat is not adequately removed by the cooling systems,  $T$ , exceeds the value of the  $T_{Cr}$ , HTS tapes enter into the highly resistive state and the fault current is diverted from the YBCO layer to the copper stabilizer layers and the former. In the presented research even distribution of  $I_{Cr}$  has been adopted for the tapes based on [3]. The superconducting phenomenon is modelled via the  $E - J$  law, given by (1), which describes the dependence of the non-linear resistivity of the YBCO layer on the critical current density,  $J_{Cr}$ , and the temperature,  $T$ . The  $J_{Cr}$  as a function of  $T$  can be derived from (2) [3,5], while the critical current,  $I_{Cr}$ , of the SC is defined as the product of the  $J_{Cr}$  and SC cross section as shown in (3):

$$\rho_{YBCO} = \frac{E_{Cr}}{J_{Cr}(T)} \cdot \left( \frac{J}{J_{Cr}(T)} \right)^{n-1} \quad (1)$$

$$J_{Cr}(T) = \begin{cases} J_{Cr0}(B) \cdot \left( \frac{T_{Cr}-T(t)^a}{T_{Cr}-T_0^a} \right) & \text{for } T < T_{Cr} \\ 0 & \text{for } T \geq T_{Cr} \end{cases} \quad (2)$$

$$I_{Cr} = J_{Cr} \cdot A_{SC} \quad (3)$$

where  $E_{Cr}$  denotes the critical electric field at which the DC current is defined and is equal to  $1 \mu\text{V}/\text{cm}$ ,  $n$  is a superconductor macroscopic property related to the steepness of the  $E - J$  law and has been set to 30 [32];  $J_{Cr0}$  is the critical current density ( $\text{A}/\text{m}^2$ ) at the initial temperature  $T_0 = 70$  (K) and the working magnetic field  $B$  (T);  $a$  has been set to 1.5 based on [4] and indicates the density exponent of the YBCO;  $A_{SC}$  ( $\text{mm}^2$ ) is the cross section of the SC.

When the HTS tapes quench, start to lose completely their superconducting properties and present high values of resistivity (higher compared to normal conductors in cryogenic conditions [33]). On that front, for protection purposes, HTS tapes are built as a composite, consisting of superconducting layers and normal conducting stabilizer materials such as copper. During the quenching conditions, the fault current is diverted into the copper stabilizer layers and the former. This is known as the current sharing process. The amount of the current diverted to the copper stabilizer layers and the former is dependent on the electrical properties of the SC at the highly resistive state and of the stabilizer/former.

The current flowing through the copper stabilizer layers and the former causes Joule heating generation which subsequently results in temperature rise. At the highly-resistive state, the resistivity of the copper stabilizer layers changes as a function of  $T$  based on (4) [3] (the resistivity of the former will be analysed in Section 2.2):

$$\rho_{Cu} = (0.0084 \cdot T - 0.4603) \cdot 10^{-8}, \quad 250 \text{ K} > T \geq 70 \text{ K} \quad (4)$$

For modelling purposes, the resistance of YBCO layer ( $R_{YBCO}$ ) and the copper stabilizer layers ( $R_{Cu}$ ) have been modelled as variable resistors connected in parallel, based on (1) and (4), respectively; the resistance of the silver ( $R_{Ag}$ ) and substrate layers ( $R_{Sub}$ ) have been neglected. However, the total thickness of the substrate and silver layers have been considered for the thermal modelling and analysis of the SC. The geometrical characteristics of the HTS tape utilized in this work are presented in Table 1 [5].

### 2.2. Structure of the SC

Based on the design of the HTS tapes presented in the previous subsection, a SC has been devised with a cross-sectional structure as depicted in Fig. 2. The SC includes three single-phase conductors contained in three separate cryostats.

Each phase consists of the copper former and several conducting layers of HTS tapes, which are wound around the former, along with

**Table 1**  
Geometrical characteristics of HTS tapes.

Parameter	Value
Thickness of YBCO layer	1 $\mu\text{m}$
Thickness of Copper layer	40 $\mu\text{m}$
Thickness of substrate layer	60 $\mu\text{m}$
Thickness of silver layer	3.8 $\mu\text{m}$
Tape width	4 mm

**Table 2**  
Geometrical characteristics of SC.

Layer	Outer radius
Steel (former tube)	16.5 mm
HTS conductor	16.64 mm
Electrical insulation	18.64 mm
HTS shield	18.78 mm
Heat insulation	21.78 mm

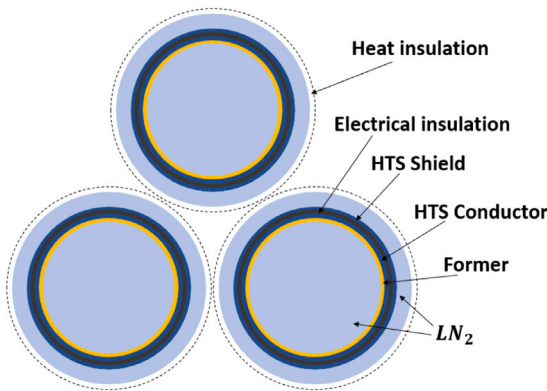


**Fig. 2.** Cross-section of the SC model.

an insulation layer and a HTS shield layer. Polypropylene Laminated Paper (PPLP) cold dielectric layer was considered between the HTS conducting and the shielding layer, acting as electric insulation, while permitting the SC to operate at relatively low temperatures. The SC cooling system is composed of a cryostat with Liquid Nitrogen ( $LN_2$ ) at 65–70 K, which is circulated in the cable loop to refrigerate the SC and operate below the  $T_{Cr}$  [3]. The former is utilized for  $LN_2$  channel. As it has already mentioned in Section 2.1 the main purpose of the former is to provide a conducting current path (along with the stabilizer layers) during the quenching and also mechanical support to the SC in order to allow the conducting layers to preserve their shape. The resistivity of the former, which is made of stainless steel, has been considered to be temperature-dependent and its value is given by (5) [4]:

$$\rho_{steel} = 1.193 \cdot 10^{-6} - 7.529 \cdot 10^{-7} \exp(-T/647.113) \quad (5)$$

The geometrical characteristics of the SC are included in Table 2. The dynamically changing equivalent resistance of the SC is dependent on the resistivity of the YBCO layer (given by (1)), the copper stabilizer layers (given by (4)) and the copper former (given by (5)) and is calculated according to (6), for all the operating stage of the SC:

$$R_{eq} = \begin{cases} R_{YBCO} & \text{for } T < T_{Cr} \text{ and } I < I_{Cr} \\ R_{YBCO} // R_{Cu} // R_{steel} & \text{for } T < T_{Cr} \text{ and } I > I_{Cr} \\ R_{Cu} // R_{steel} & \text{for } T > T_{Cr} \text{ and } I > I_{Cr} \end{cases} \quad (6)$$

The per-unit length self and mutual capacitances,  $C$ , and inductances,  $L$ , have been calculated based on the general formulation provided in [34], considering the conducting layers and the shield layers of each phase. Specifically, the helically wound HTS tapes around the former, result in the generation of an axial magnetic field which

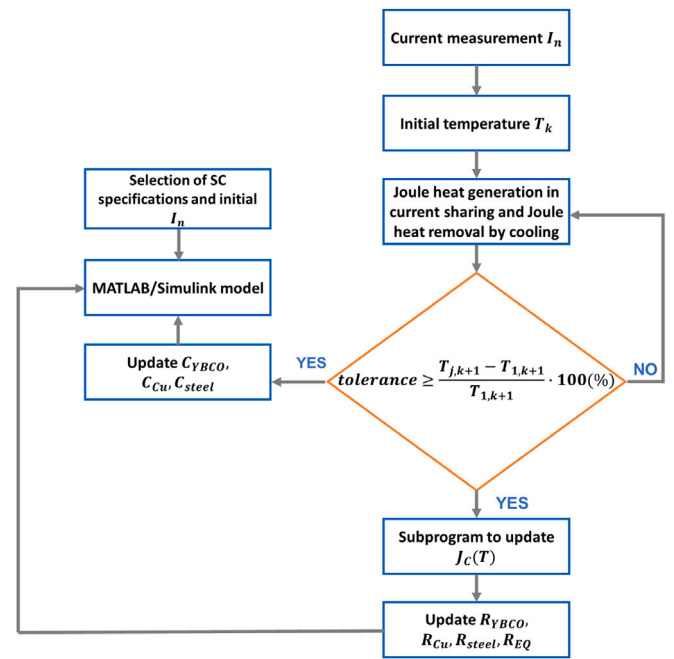


**Fig. 3.** Overview of the electro-thermal modelling.

subsequently causes a solenoid effect. The impact of the solenoid effect on the  $L$  calculation has been considered based on the approach proposed in [35].

### 2.3. Thermal modelling

In the presented research, the electro-thermal analogy is employed in order to simplify the coupling between the thermal and electrical phenomena. Therefore, currents are translated into Joule heating and the resulting temperature variations into changes to the properties of the SC. The temperature-dependent properties of the SC include: (i) the heat capacity,  $C$ , of the YBCO layer, the copper stabilizer layers and the former, which represents the generated Joules per one Kelvin degree [5], (ii) the critical current density,  $J_{Cr}$ , given by (2) and (iii) the resistivity of the YBCO layer, the copper stabilizer layers and the former given by (1), (4) and (5), respectively. The modelling methodology developed by the authors in [5] has been adopted and enhanced to include the temperature-dependance of the SC properties. Fig. 3 presents an overview of the modelling process, as developed in Matlab/Simulink.

To achieve high-fidelity temperature-dependent modelling, the calculation of the temperature at each time step is based on an iterative process and is dependent on (i) the temperature,  $T_k$ , from the previous time step, (ii) the current,  $I_k$ , flowing through the SC, and (iii) the equivalent resistance,  $R_{eq}$ , of the SC. An error tolerance is also applied in the thermal model which determines the settling temperature at each time step, as given by (7):

$$tolerance \geq \frac{T_{j,k+1} - T_{1,k+1}}{T_{1,k+1}} \cdot 100(\%) \quad (7)$$

At the end of each time-step, the temperature-dependent properties of the SC are updated accordingly to the  $T_k$  value. In the developed model, the tolerance value has been set to 0.01%.

### 3. Power system modelling & SC fault characterization

Prior to the introduction of the developed fault location method, it is important to understand how the SCs would be integrated to the wider power system and investigate their response to faults.

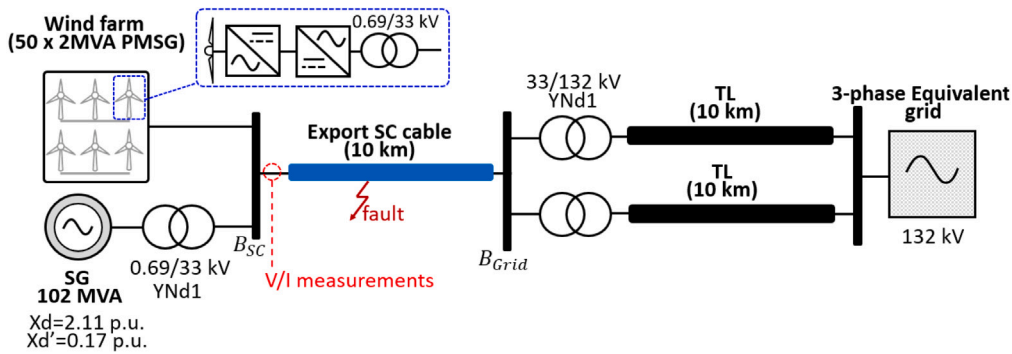


Fig. 4. Test network.

**Table 3**  
Parameters of the SC.

Parameter	Value
Number of tapes $n_{tapes}$	25
Operating temperature $T_0$	70 K
Critical temperature $T_{Cr}$	92 K
Critical current per tape $I_{Cr}$	250 A
Cable length $l$	10 km
Rated voltage $V$	33 kV
Rated capacity $S$	202 MVA

### 3.1. Power system under test

The transient performance of the SCs, has been investigated by conducting Electromagnetic Transient (EMT) simulation studies. For this purpose, the power system under test, depicted in Fig. 4, has been developed in Matlab/Simulink.

The test network consists of an equivalent transmission network (represented by a voltage source in series with an impedance), connected to bus  $B_{Grid}$  and two different generation units (i.e., a SG and a CIG) both connected to bus  $B_{SC}$ . The SG unit has nominal capacity of 102 MVA. For the modelling of the SG, a standard salient pole synchronous machine has been utilized along with the integration of Automatic Voltage Regulator (AVR), Power System Stabilizer (PSS) and over-excitation limiter. The CIG unit (i.e., a wind farm cluster) has total capacity of 100 MVA and constitutes of permanent magnet SGs connected via CIGs. The incorporated control scheme for the converters is the standard d-q axis current injection (DQCI).

A 10 km SC has been integrated between  $B_{Grid}$  and  $B_{SC}$  at 33 kV for the power transmission from the generation units to the wider electrical grid. Measurement of three-phase voltages and currents are captured at the one end of the SC as can be seen in Fig. 4. The parameters of the developed SC are presented in Table 3.

### 3.2. Transient performance of the SC

The response of the AC SC was investigated under different fault conditions by conducting an iterative simulation-based fault analysis. The time step of the simulation is equal to  $50 \cdot 10^{-6}$  s (20 kHz). For this purpose, all fault types have been simulated, accounting for three-phase (3-Ph), three-phase to ground (3-Ph-G), phase-to-phase (Ph-Ph), phase-to-phase to ground (Ph-Ph-G) and phase-to-ground (Ph-G), considering different values of fault resistance  $R_f$ , (within the range of 0  $\Omega$  up to 300  $\Omega$ ), and varying fault position. Two representative fault scenarios have been selected for the transient analysis of the SC in order to demonstrate the quenching phenomenon and the impact of the  $R_f$  on the quenching of the HTS tapes. Indicatively, Fig. 5 presents the response of the SC during a Ph-Ph-G solid fault, occurring at 40% of the SC length triggered at  $t = 3.06$  s.

During the steady-state, pre-fault conditions, SC operates at  $T_o$ , the resistance of the YBCO layer is approximately zero, providing a current path with approximately zero losses. The current flowing through the YBCO layer is shown in Fig. 5a. The fault is applied at  $t = 3.06$  s. When the value of the fault current reaches the value of the  $I_{Cr}$ , the quenching process of the HTS tapes is initiated and the SC develops a longitudinal resistive voltage [33]. Under these conditions, the fault current starts flowing through the copper stabilizer layers and the former (current indicated as  $I_{shunt}$  in Fig. 5b) at  $t = 3.064$  s. The fault current diversion results in an increase in the resistivity of copper stabilizer layers and former based on (4) and (5), respectively. Fig. 5c shows the change in the equivalent resistance of the SC (which reaches values over 8  $\Omega$ ). Due to the increase in the resistance of the SC during the transition to the highly resistive state, the magnitude of the perspective fault current is reduced. Fig. 5d demonstrates the resulting rise in the temperature of the SC, which reaches values higher than the critical temperature  $T_{Cr} = 92$  K.

Furthermore, for the design of the fault location scheme, it is essential to consider resistive faults, which are anticipated to affect the resulting voltage and current signatures. Fig. 6 depicts the response of the SC under a Ph-Ph-G with  $R_f = 15 \Omega$ , occurring at 40% of the SC length. As depicted in Fig. 6a and Fig. 6b, during a resistive fault, the HTS tapes do not quench as the resulting fault current is very low. The YBCO layer remains to superconducting state and therefore there is no current sharing with the copper stabilizer layers and the former. Subsequently, the equivalent resistance of the SC is approximately zero (Fig. 6c) and the temperature is sustained to the operating temperature (i.e.,  $T_0 = 70$  K). These results indicate that an increase in  $R_f$ , leads to reduced prospective fault currents (lower than the  $I_{Cr}$ ) and the quenching process is significantly compromised.

The above analysis highlights that the deployment of the SC introduces a dynamically varying equivalent impedance of the SC, which affects the resulting fault current signatures and the fault resistance presence jeopardizes the quenching of the HTS tapes. Such behaviour introduces additional challenges to fault management of SCs, accounting for protection and fault localization.

## 4. Proposed fault location algorithm

The developed fault location scheme utilizes single-ended current and voltage signatures from the SC, which are available locally from the measuring equipment (there is no need for synchronized measurements from both ends). The signals are imported to a spectral analysis tool and are transformed from time-domain to time-frequency domain. Image analysis techniques combined with DL tools are deployed to estimate the fault location along the SC length.

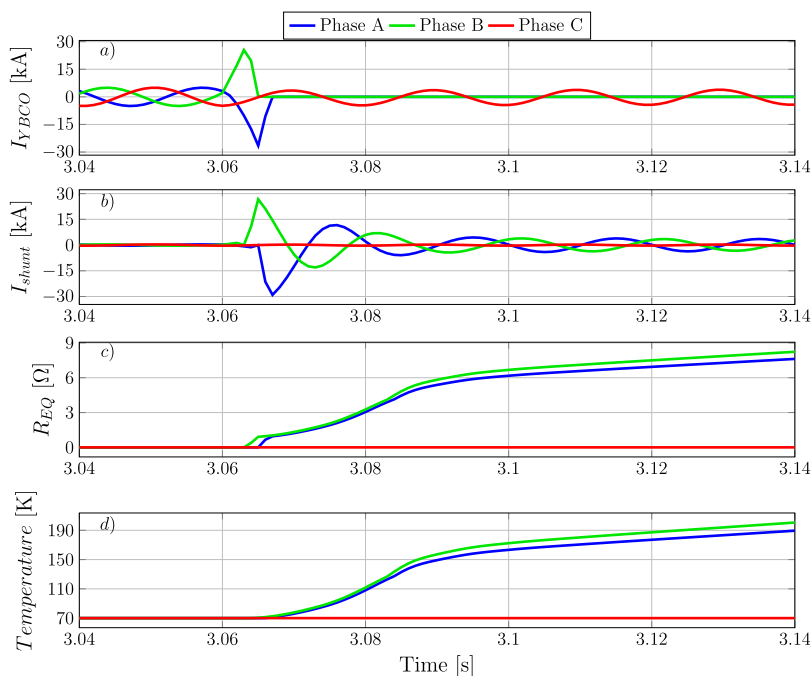


Fig. 5. SC performance under a Ph-Ph-G solid fault at 40% of SC length: (a) Currents through YBCO, (b) Currents through copper stabilizer layers and former, (c) Equivalent resistance of SC, (d) Temperature of SC.

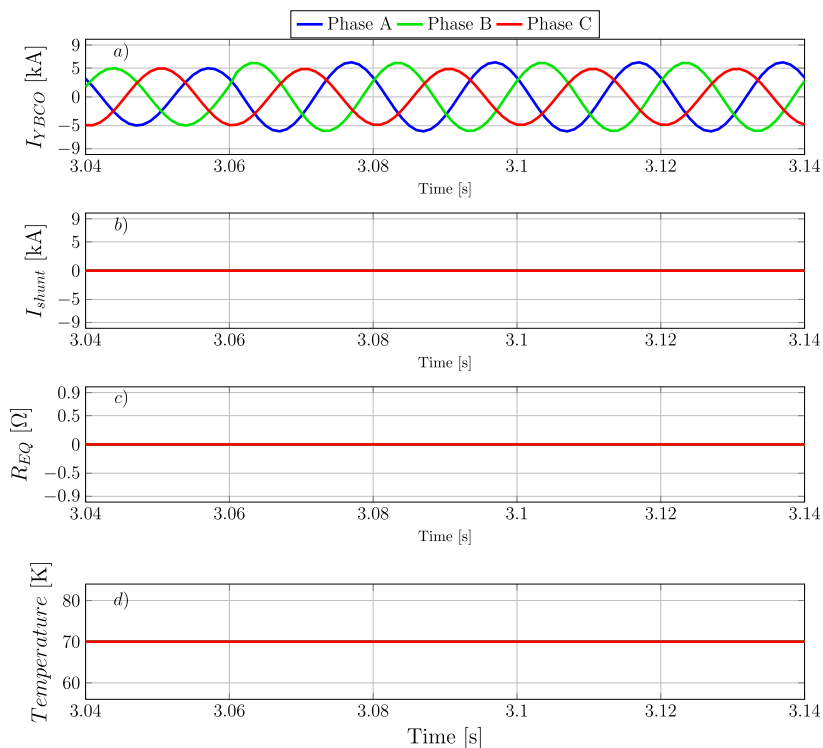


Fig. 6. SC performance under a Ph-Ph-G fault with  $R_f = 15 \Omega$  at 40% of SC length: (a) Currents through YBCO, (b) Currents through copper stabilizer layers and former, (c) Equivalent resistance of SC, (d) Temperature of SC.

#### 4.1. Stages of the proposed faults location scheme

A four-stages methodology has been incorporated for the development of the fault location scheme as illustrated in Fig. 7. The following subsections provide a detailed explanation of each stage. To aid the clarity of the description, an investigated scenario of a 3-Ph-G solid fault, at 50% along the SC length is discussed.

##### 4.1.1. Stage I - signal acquisition

Measurements of three-phase voltages and currents from one end of the SC are captured with sampling frequency of 20 kHz. The investigation of different sampling frequency values is presented in Section 5.4. Relevant analysis conducted revealed that five cycles (one pre-fault and four during the fault) of data would be more than adequate for this application. The recorded data are filtered via relevant anti-aliasing

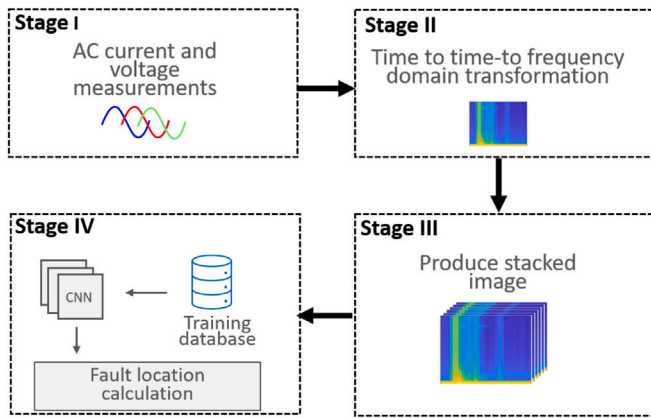


Fig. 7. Schematic diagram of the CNN-based fault location scheme.

filters, normalized and packaged into appropriate time windows to be processed for spectral analysis at the following stage of the algorithm. Fig. 8 shows the obtained time domain fault current and voltage waveforms for the tested fault case.

#### 4.1.2. Stage II - signal to image transformation

At this stage, the time domain signals (i.e., voltages and currents), are transformed to time–frequency domain in order to produce 2D images. Specifically, the fault current and voltage waveforms, are utilized to produce the corresponding spectrograms, which are plotted within a time–frequency plane. The image transformation has been selected as a powerful feature extraction tool in order to reveal hidden information in the time domain data.

To compute the time-dependent spectrum, the non-stationary signal is divided into shorter segments of equal length. The length of each segment, specifies the time resolution and must be smaller or equal to the signal duration. In the developed method, each signal has been divided into 8 segments of 250 samples each, with 50 samples overlap. Then, a window-based Short-Time Fourier Transform (STFT) is applied on each segment to compute the corresponding spectrum [36]. Finally, the segments spectra are concatenated to construct the spectrogram [36], which enables the localization of frequency in time, by means of magnitude-dependent colourmap. Fig. 9 shows the spectrograms derived from the three-phase currents and voltages of Fig. 8.

#### 4.1.3. Stage III - image pre-processing

The six resulting spectrograms with dimension  $(H \times W)$ , where  $H$  is the height and  $W$  is the width of the image, are stacked together to form a multi-layer image with dimensions  $(L \times H \times W)$ . Parameter  $L$  denotes the number of over-layered images which corresponds to  $L = 6$  in this application. The resulting stacked image will be used as input to the DL model at the following stage. Fig. 10 represents a stacked image stemming from the over-laying of the spectrograms depicted in Fig. 9.

#### 4.1.4. Stage IV - estimation of fault location

At the final stage of the algorithm the fault location is estimated. The stacked images for all the fault scenarios are utilized as inputs to the DL-based network. The fault localization on the SCs is formed as a regression problem, where the DL network provides the value of the estimated fault location at its output.

Taking as a reference the bus  $B_{SC}$ , the error of the fault localization can be calculated according to (8):

$$error_{FL}[\%] = \left| \frac{C_F - A.C_F}{L_{SC}} \right| \cdot 100(\%) \quad (8)$$

where  $C_F$  is the predicted fault location from the DL-based network,  $A.C_F$  is the actual fault location and  $L_{SC}$  is the SC total length.

A comprehensive analysis of different DL-based networks has been conducted and eventually the results revealed that CNN are the most robust and effective algorithms for image processing. Furthermore, the motivation of utilizing CNN algorithm is their ability to capture sequence patterns in the input data. The detailed analysis of the developed CNN is presented in the following subsections.

## 4.2. Convolution Neural Network

CNN is a type of Artificial Neural Network (ANN) which presents outstanding performance when dealing with image analysis tasks. CNN combines the ability of feature extraction and pattern recognition and is capable of preserving the spatial or positional relationships between input data points. Therefore, CNNs have been widely applied to power systems applications for fault diagnosis [23]. Typically, a CNN is constructed by an input layer, a series of convolution layers with filters (kernels), the pooling and the fully connected (FC) layers.

The convolution layer is utilized to extract local features of the input images, by applying the convolution operation. In principle, convolution operation is a linear operation of multiplication and addition of the convolution filters (kernels) with the corresponding elements of the input feature map. The first convolution layer is utilized for the extraction of the low-level features of the input images accounting for image edges, gradient orientation, etc. With the addition of more convolution layers the high-level features are captured as well, providing an overall understanding of the input images. If the input data are formed to matrix  $n \times n$  and the convolution kernel is  $k \times k$ , the output is a  $m \times m$  matrix and (9) is satisfied [37]:

$$m = n - k + 1 \quad (9)$$

The convolution operation is based on the formula described in (10):

$$Y_o^l = f\left(\sum_{i \in m} Y_o^{l-1} \cdot K_{io}^l + b^l\right) \quad (10)$$

where  $Y_o^l$  denotes the output of the  $l$ th layer;  $Y_o^{l-1}$  is the input of the  $l$ th layer;  $B$  is the offset;  $K$  denotes the kernel element and  $f$  is the activation function. In the presented research ReLU has been selected as activation function for the convolution layers.

The purpose of the pooling layer is to scale data from the previous layer, reduce the data dimension and consequently reduce computation time and prevent overfitting [30]. The output of the convolution and the pooling layer is fed into a linear fully connected feed forward layer, where the associated activation function provides the desirable output.

## 4.3. Selection of CNN model

For the development of the fault location scheme several well-known CNN architectures, proposed by the computer vision community, have been evaluated in order to select the one which provides the most accurate fault location estimation [38]. The fault scenarios obtained through the simulation analysis conducted in Section 3.2, were utilized to produce the corresponding spectrograms and create the training data base. For the data pre-processing the PyTorch open source machine learning library has been utilized. It is worth reiterating that the CNN models were trained and tested for all fault types, for different values of  $R_f$  and varying fault location with an increment of 10% of the SC length. Consequently, a data set of 415 transient events has been created, from which 60% was used to train the CNN models, 20% was used for validation purposes, while the remaining 20% for testing purposes.

For the selection of the (i) optimum hyperparameters, accounting for the batch size and the learning rate, and (ii) the best training model of each CNN model, the Grid-Search (GS) five-fold Cross-Validation (CV) technique has been adopted. Specifically, the CNN models have been trained and validated for different combinations of hyperparameters. To provide a deeper insight, five-fold CV technique works by

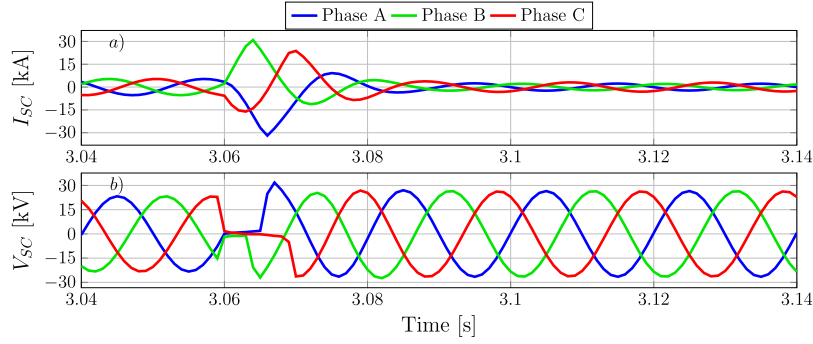


Fig. 8. Voltage and current signatures during a 3-Ph-G solid fault at 50% of SC length: (a) three phase currents, (b) three phase voltages.

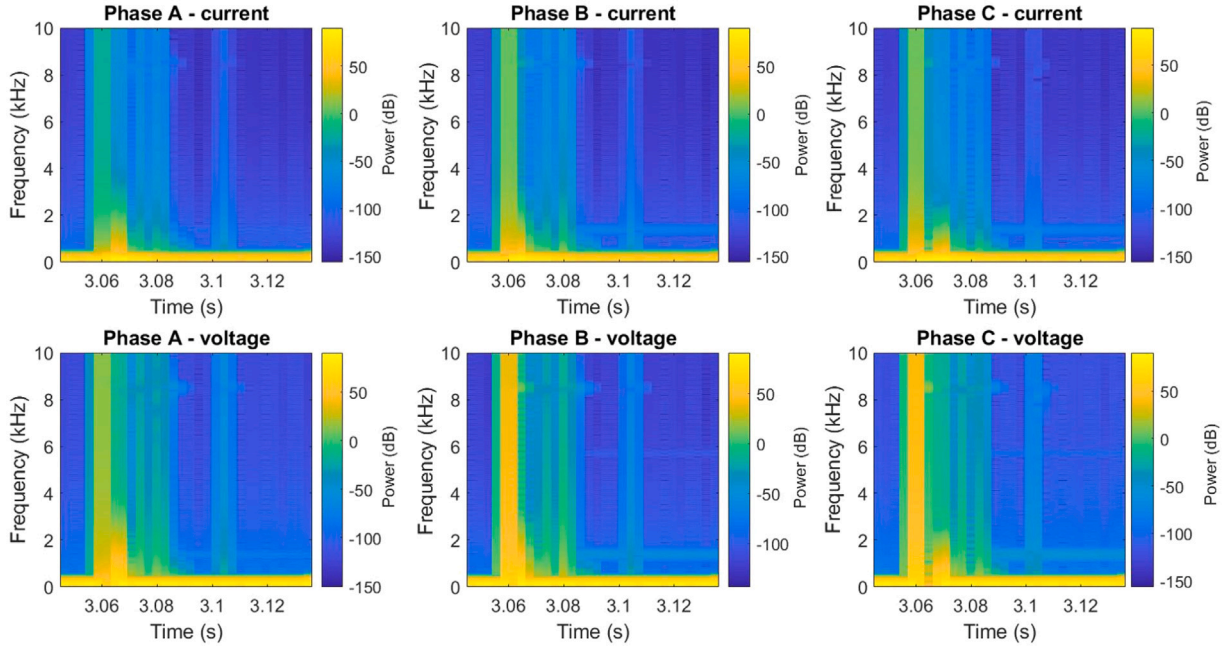


Fig. 9. Current and voltage spectograms for a 3-Ph-G solid fault at 50% of SC length.

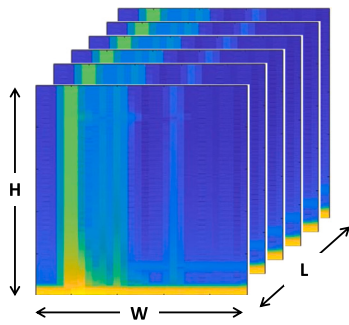


Fig. 10. Stacked image.

initially splitting the dataset into five folds (i.e., subsets). During each iteration four folds are utilized for the training process and the remaining one fold for the validation. Therefore, each CNN model is trained and validated five times, considering each time different combinations of hyperparameter. The optimum combination of the hyperparameters gives the model with the best performance and is selected according to the five-fold CV score (i.e., average of the scores derived by each subset). In this research the mean fault location estimation error, has

been considered as five-fold CV score and it is given by (11):

$$\overline{error}_{FL}[\%] = \frac{1}{N} \sum_{i=0}^N \left| \left( \frac{\hat{y}_i - y_i}{L_{SC}} \right) \right| \cdot 100(\%) \quad (11)$$

where  $\hat{y}_i$  corresponds to the estimated fault location,  $y_i$  denotes the actual fault location and  $N$  is the total number of data points.

The CNN models have been trained by the back propagation gradient descent method and the Adam optimizer utilized as the optimization algorithm. For each CNN model the combination with the lowest  $\overline{error}_{FL}$  has been selected. At the next stage the final trained CNN models (with the best combination of the hyperparameters) were tested on the testing dataset, utilizing again the  $\overline{error}_{FL}$  as evaluation metric. The obtained results are presented in Table 4.

It is worth highlighting that the Inception-v3 CNN model with the following final hyperparameters: batch size = 4, learning rate = 0.001, presented the lowest  $\overline{error}_{FL}$  and subsequently was selected as the best CNN model.

The layers of the Inception-v3 model are demonstrated in Table 5, along with the input size of each layer. The input image is  $510 \times 580$  with 6 channels. At the output of the developed CNN model there is a fully-connected layer which yields the numerical value of the predicted fault location, as a percentage of the SC length.

**Table 4**  
Tested CNN models and their performance on the testing dataset.

CNN model	$\overline{error}_{FL}(\%)$
Inception-v3	0.70
ResNet50	3.16
ResNet101	2.76
ResNet152	3.02
Densenet	4.20
VGG11	0.97
VGG13	1.25
VGG16	0.88
VGG19	0.98

**Table 5**  
The outline of the proposed CNN model.

Layer type	Input size
Conv	$510 \times 580 \times 6$
Conv	$254 \times 289 \times 32$
Con padded	$252 \times 287 \times 32$
Pool	$252 \times 287 \times 64$
Conv	$125 \times 143 \times 64$
Conv	$123 \times 141 \times 80$
Conv	$61 \times 70 \times 192$
3× Inception	$61 \times 70 \times 288$
5× Inception	$30 \times 34 \times 768$
2× Inception	$14 \times 16 \times 1280$
Pool	$14 \times 16 \times 2048$
Fully-connected	$1 \times 1 \times 2048$

## 5. Performance evaluation of proposed fault location scheme

To examine the robustness of the proposed fault location algorithm, its performance has been evaluated under the occurrence of different fault scenarios with varying fault location. Furthermore, the impact of the  $R_f$ , the small increments of fault location, the fault inception angle, the noise and the sampling frequency on the effectiveness of the proposed scheme has been investigated. The simulation-based results are analysed in the following subsections.

### 5.1. Fault location results

To achieve an overall performance assessment of the proposed scheme, its fault location estimation capability was evaluated based on additional faults, which have not been distributed equally along the SC length. It shall be highlighted that these fault locations do not belong to initial dataset. The purpose for this is that any fault location scheme must present increased generalization capability and be able to provide accurate fault locations estimation with inputs not necessarily similar to the training dataset. Table 6 shows the results of the fault location estimation by presenting the values of the actual fault location, the predicted fault location at the CNN output along with the  $error_{FL}$  derived by (8). The results validate the effectiveness of the proposed scheme. It is important to highlight that the CNN model achieves accurate fault location estimation even in the case of the close-up faults (i.e, faults occurring close to the head or end the SC) and under the influence of highly resistive faults. Based on the obtained results in Table 6 the lowest  $error_{FL}$  is 0.01% and the  $\overline{error}_{FL}$  of the proposed algorithm for the presented scenarios is 0.34%.

Furthermore, Fig. 11 presents the performance of the proposed fault location scheme under the influence of 3-Ph-G faults occurred at every 5% of SC length for different values of  $R_f$ . The sensitivity analysis with respect to SC length shows that the  $error_{FL}$  lies within the range of 0.009% and 1.108% and consequently verifies the increased accuracy in the fault location estimation.

### 5.2. Effect of small increments of fault distance

An incremental change of 10 m in fault location has been investigated in order to assess the sensitivity of the proposed scheme to small variations of the actual fault position. Specifically, the effectiveness of the fault location scheme has been evaluated for fault positions within the range of 5.9 km to 6.1 km with steps of 10 m. By changing the fault location by a small increment of 10 m, the influence of randomly varied sampling instant is also investigated. Fig. 12 shows the percentage fault location errors derived for this range of the fault positions during a 3-Ph-G solid fault. It is evident that the  $error_{FL}$  fluctuates between 1.2% to 0.1% which confirms the capability of the algorithm to provide high estimation accuracy for very small increments of fault location (in the range of 10 m).

### 5.3. Effect of fault inception angle

In order to scrutinize the performance of the CNN algorithm under different values of fault inception angles  $\delta_f$ , a Ph-Ph-G fault has been applied at 65% of the SC length for  $\delta_f$  from 0 up to 180 degrees with step of 30 degrees. The main scope of this investigation is to evaluate the immunity of the fault location algorithm to variations in the  $\delta_f$  and subsequently in the time instant in the electric cycle when the fault occurs. The acquired results are presented in Fig. 13 and confirm that the estimation capability of the proposed algorithms is not affected by the changes in fault inception angle, yielding  $error_{FL}$  equal to 0.27% for all the investigated cases.

### 5.4. Effect of sampling frequency

The fault location scheme has been additionally tested with respect to the sampling frequency. In particular, the performance of the proposed technique was evaluated for a series of testing scenarios, considering sampling frequencies from 20 kHz (i.e., the selected sampling frequency for the presented studies) and lower down to the 5 kHz. Table 7 shows the resulting  $error_{FL}$  from the conducted studies for some representative scenarios. As it can be seen the fault location estimation accuracy is affected by the value of the sampling frequency. As the value of the sampling frequency decreases below the 20 kHz, the  $error_{FL}$  increases and the performance of the developed scheme is jeopardized. The results reveal the requirements and the limitations of the developed method regarding the sampling frequency. For practical SC applications, the lowest sampling frequency which would lead to a precise fault location estimation is 20 kHz.

### 5.5. Effect of noise

In practical deployment of SCs, noise can be caused by power quality issues, transducers or modulators and constitutes one of the most adverse factors which can potentially affect the accuracy of the fault location schemes. Furthermore, many studies have been focused on the compensation of the Current Transformer (CT) saturation on the performance of fault location schemes [39,40]. In the presented work the investigation of CT saturation phenomenon is out of scope, as it is anticipated that during the practical implementation of the proposed scheme, more advanced measuring solutions can be utilized (i.e., fibre optics) [41]. To exclude the ideal measuring capability and assess the robustness of the proposed algorithm under these conditions, the time domain current and voltage measurements of the testing scenarios have been subjected to artificial noise. Indicatively, Fig. 14 demonstrates the spectrograms of Phase A current resulting from time domain current signal without noise and with 100 dB signal-to-noise ratio (SNR), respectively, for a 3-Phase-G solid fault at 5.3 km of SC length. Table 8 presents the obtained  $error_{FL}$  with respect to increasing noise amplitude for 6 representative fault scenarios from Table 6 (scenarios with the lowest and highest  $error_{FL}$  prior to the noise addition).

**Table 6**  
Fault location  $error_{FL}$  for the CNN-based fault location scheme.

Fault type	$R_f$ ( $\Omega$ )	$A.C_F$ (km)	$C_F$ (km)	$error_{FL}$ (%)	Fault type	$R_f$ ( $\Omega$ )	$A.C_F$ (km)	$C_F$ (km)	$error_{FL}$ (%)	Fault type	$R_f$ ( $\Omega$ )	$A.C_F$ (km)	$C_F$ (km)	$error_{FL}$ (%)
3-Ph-G	0	0.4	0.36	0.4	3-Ph	0	0.52	0.559	0.39	Ph-Ph-G	0	7.8	7.9	1
3-Ph-G	0	2.2	2.212	0.12	3-Ph	0	2.39	2.397	0.07	Ph-Ph-G	0	2.4	2.48	0.8
3-Ph-G	0	8.7	8.62	0.8	3-Ph	0	7.76	7.77	0.1	Ph-Ph-G	0	2.6	2.62	0.2
3-Ph-G	0	9.96	9.961	0.01	3-Ph	0	6.6	6.622	0.22	Ph-Ph-G	0	8.95	8.915	0.35
3-Ph-G	2	5.2	5.31	1.1	3-Ph	2	3.13	3.149	0.19	Ph-Ph-G	2	9.97	9.865	1.05
3-Ph-G	2	8.4	8.41	0.1	3-Ph	2	7.14	7.112	0.28	Ph-Ph-G	2	0.91	0.816	0.94
3-Ph-G	5	8.7	8.72	0.2	3-Ph	5	9.9	9.908	0.08	Ph-Ph-G	5	6.3	6.29	0.1
3-Ph-G	5	2.1	1.998	0.2	3-Ph	5	7.97	7.915	0.55	Ph-Ph-G	5	0.9	0.815	0.85
3-Ph-G	15	3.6	3.69	0.9	3-Ph	15	4.99	5.1	1.1	Ph-Ph-G	15	1.8	1.75	0.5
3-Ph-G	15	4.2	4.25	0.5	3-Ph	15	8.37	8.35	0.2	Ph-Ph-G	15	2.71	2.627	0.83
3-Ph-G	200	3	3.009	0.09	3-Ph	200	2.48	2.448	0.32	Ph-Ph-G	200	1.61	1.54	0.7
3-Ph-G	200	9.2	9.221	0.21	3-Ph	200	5.98	5.978	0.02	Ph-Ph-G	200	9.52	9.487	0.33
3-Ph-G	250	9.98	9.981	0.01	3-Ph	250	9.13	9.161	0.31	Ph-Ph-G	250	4.48	4.592	1.12
3-Ph-G	250	0.98	9.923	0.57	3-Ph	250	2.99	3.05	0.6	Ph-Ph-G	250	1.13	1.098	0.32
3-Ph-G	300	0.14	0.146	0.06	3-Ph	300	0.45	0.454	0.04	Ph-Ph-G	300	0.02	0.024	0.04
3-Ph-G	300	6.17	6.156	0.14	3-Ph	300	4.32	4.441	0.9	Ph-Ph-G	300	8.92	8.941	0.21

Fault type	$R_f$ ( $\Omega$ )	$A.C_F$ (km)	$C_F$ (km)	$error_{FL}$ (%)	Fault type	$R_f$ ( $\Omega$ )	$A.C_F$ (km)	$C_F$ (km)	$error_{FL}$ (%)
Ph-Ph	0	1.64	1.644	0.04	Ph-G	0	6.9	6.924	0.24
Ph-Ph	0	2.67	2.648	0.22	Ph-G	0	1.81	1.79	0.2
Ph-Ph	0	7.45	7.464	0.14	Ph-G	0	2.7	2.68	0.2
Ph-Ph	0	9.39	9.393	0.03	Ph-G	0	3.33	3.324	0.06
Ph-Ph	2	6.49	6.46	0.3	Ph-G	2	2.25	2.264	0.14
Ph-Ph	2	8.15	8.151	0.01	Ph-G	2	5.5	5.618	1.18
Ph-Ph	5	9.21	9.131	0.79	Ph-G	5	6.38	6.37	0.1
Ph-Ph	5	5.14	5.141	0.01	Ph-G	5	7.31	7.23	0.8
Ph-Ph	15	4.29	4.275	0.15	Ph-G	15	9.79	9.781	0.09
Ph-Ph	15	7.11	7.116	0.06	Ph-G	15	1.11	1.09	0.2
Ph-Ph	200	0.71	0.693	0.17	Ph-G	200	4.4	4.418	0.18
Ph-Ph	200	9.54	9.561	0.21	Ph-G	200	9.99	9.96	0.3
Ph-Ph	250	1.38	1.401	0.21	Ph-G	250	3.99	3.988	0.02
Ph-Ph	250	9.79	9.831	0.41	Ph-G	250	8.48	8.501	0.21
Ph-Ph	300	0.05	0.052	0.02	Ph-G	300	4.11	4.108	0.02
Ph-Ph	300	6.99	6.954	0.36	Ph-G	300	0.44	0.437	0.03

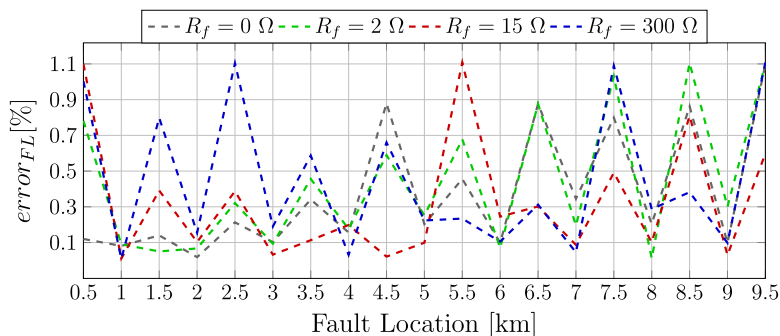


Fig. 11. Absolute percentage of fault location error for 3-Ph-G faults at each 5% of SC length for different values of fault resistance  $R_f$ .

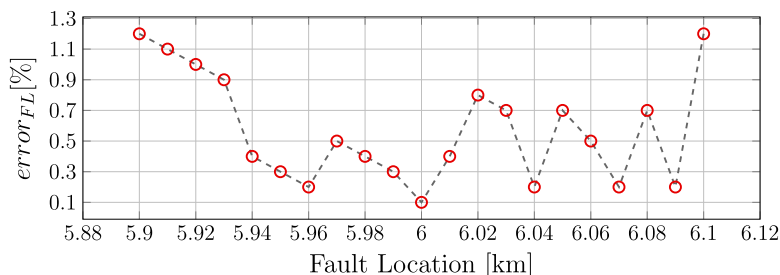


Fig. 12. Absolute percentage of fault location error with respect to 10 m increment of fault distance.

It can be observed that the increase in the noise level (higher level of noise corresponds to lower value of dB) has a slight impact on the  $error_{FL}$ . Specifically, the higher  $error_{FL}$  is reported for SNR 30 dB. However, the resulting values of  $error_{FL}$  remain within acceptable limits without deteriorating the fault location estimation accuracy.

Therefore, the proposed fault location scheme presents immunity against the additive noise to the time domain measurements of the testing scenarios. Furthermore, this analysis highlights the capability of the proposed algorithm to deal with more difficult testing scenarios and subsequently confirms that the developed CNN-based scheme does not

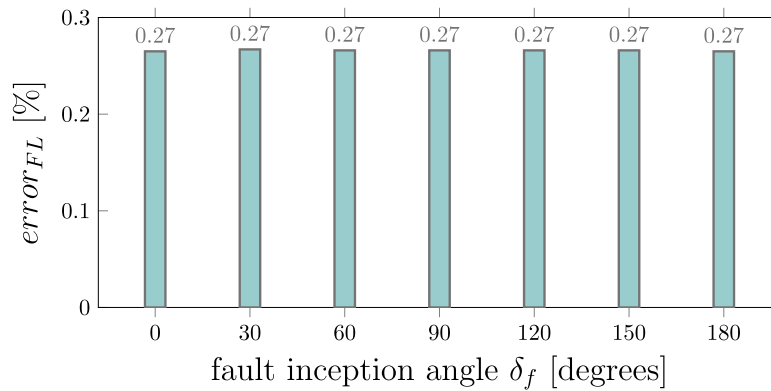


Fig. 13. Impact of fault inception angle  $\delta_f$  to fault location accuracy.

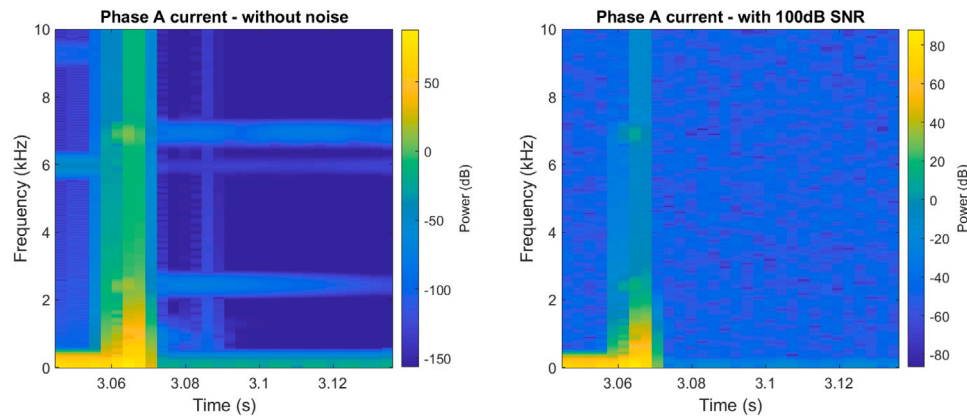


Fig. 14. Spectrograms obtained from time domain current measurements with and without noise.

Table 7

Fault location  $error_{FL}$  of representative scenarios for different sampling frequency.

Fault type	$R_f$ ( $\Omega$ )	$A.C.F$ (km)	20 kHz	10 kHz	5 kHz
3-Ph-G	0	5.20	0.022	0.68	1.100
3-Ph-G	50	9.41	0.063	0.855	1.205
3-Ph-G	200	1.30	0.080	0.970	1.381
3-Ph	300	8.10	0.621	0.882	0.991
Ph-G	2	6.30	0.132	0.941	1.230
Ph-G	0	2.11	0.041	0.449	0.942
Ph-G	150	4.70	0.048	0.559	1.082
Ph-Ph-G	0	7.90	0.012	0.688	0.921
Ph-Ph	50	3.80	0.270	0.721	1.133
Ph-Ph	0	3.22	0.032	0.510	0.994

Table 8

Fault location  $error_{FL}$  of representative scenarios with respect to additive noise on the testing scenarios.

Fault type	$R_f$ ( $\Omega$ )	$A.C.F$ (km)	Without noise	100 dB	60 dB	30 dB
3-Ph-G	0	8.80	0.010	0.056	0.107	0.200
3-Ph	2	5.20	1.100	1.130	1.191	1.286
Ph-Ph-G	0	7.80	1.000	1.056	1.109	1.198
Ph-Ph	300	0.02	0.040	0.091	0.147	0.242
Ph-G	2	5.50	1.180	1.228	1.289	1.210
Ph-G	250	3.99	0.020	0.073	0.154	0.253

face over-fitting issues and presents enhanced generalization capability.

### 5.6. Random masking and noise at the training dataset

In order to further evaluate the generalization capability of the proposed algorithm, data perturbation techniques were applied to the

time–frequency domain signals of the training dataset. Those perturbation techniques include the random masking and the addition of random noise. Specifically, the spectrograms obtained at the Stage III of the algorithm, have been subjected to masking, by hiding portions of the image/spectrogram, and simultaneously to image noise.

Random masking is a widely used technique for computer vision applications [42,43], according to which small patches of the input image (the spectrograms in the presented work) are masked and set to zero during the training process. This random removal of information prevents the developed algorithm from being overly dependent on certain features of the input. Additionally, the additions of random image noise during the training process can be utilized to increase the variability of the training dataset and mitigate the over-fitting of the algorithm to the training dataset.

The  $\overline{error}_{FL}$  of the CNN-based fault location scheme on the testing dataset (i.e., considering the random masking and the image noise during the training process) has been found equal to 0.75%, which is very close to that reported in Table 4 (considering the initial model without perturbation techniques). Furthermore, the performance of the CNN algorithm, with the random masking and the image noise, has been assessed based on the previously unseen fault scenarios reported on Table 6, similarly to the initial model. Some representative cases are demonstrated in Table 9. The results revealed that the  $error_{FL}$  for each scenario is low and therefore the fault location estimation accuracy remains high. Furthermore, the values of the resulting  $error_{FL}$  for the investigated scenarios are very close to those resulting from the initial model (which does not consider the perturbation techniques during the training process). Specifically, no notable improvement has been reported regarding the fault location estimation accuracy and for most of the cases the initial model provides more accurate fault location estimation. For the investigated scenarios presented in Table 9,

**Table 9**

Fault location  $error_{FL}$  of representative scenarios considering perturbation techniques during the training process.

Fault type	$R_f$ ( $\Omega$ )	$A.C_f$ (km)	$C_f$ (km)	$error_{FL}$ (%)
3-Ph-G	0	8.7	8.61	0.90
3-Ph-G	2	3	3.095	0.95
3-Ph-G	250	9.98	9.979	0.01
3-Ph-G	300	6.17	6.157	0.13
3-Ph-G	5	2.1	2.122	0.22
3-Ph	5	9.9	9.892	0.08
3-Ph	250	9.13	9.087	0.43
3-Ph	0	7.76	7.739	0.21
3-Ph	2	3.13	3.148	0.18
3-Ph	0	2.39	2.384	0.06
Ph-Ph-G	5	6.3	6.307	0.07
Ph-Ph-G	0	2.6	2.572	0.28
Ph-Ph-G	2	9.97	9.879	0.91
Ph-Ph-G	0	7.8	7.910	1.10
Ph-Ph-G	200	9.52	9.475	0.45
Ph-Ph	2	8.15	8.153	0.03
Ph-Ph	5	5.14	5.141	0.01
Ph-Ph	2	6.49	6.456	0.34
Ph-Ph	15	7.11	7.102	0.08
Ph-Ph	15	4.29	4.272	0.18
Ph-G	0	2.7	2.690	0.10
Ph-G	0	6.9	6.918	0.18
Ph-G	0	1.81	1.787	0.23
Ph-G	5	6.38	6.395	0.15
Ph-G	200	9.99	9.951	0.39

the  $\overline{error_{FL}}$  for the CNN algorithm with the perturbation techniques during the training process is 0.30% and for the initial CNN algorithm (i.e., without the perturbation techniques during the training process) is 0.25%. Consequently, this analysis confirms that the initial model has adequate generalization capability, does not overfit to the training dataset and removes the need for perturbation techniques during the training process.

## 6. Comparative analysis with other data-driven algorithms

The effectiveness of the developed fault location scheme has been further validated by comparing its performance with another widely used data-driven algorithm in power system applications. Specifically, the LSTM algorithm has been selected for comparison purposes as it is a widely adopted artificial Recurrent Neural Network (RNN) for fault diagnosis applications [44]. LSTM models are well-suited to processing sequence of data (i.e, time-series data) and adaptively learn the dynamic information of the input data by non-linear gating units. Their main advantage is that they extract temporal correlation of time series data (serial correlations) and parallel dependencies (correlations of the input features) [24], while control the amount of information that needs to be retained.

### 6.1. Stages of the LSTM algorithm

The three-stage algorithm developed for the estimation of the fault location on the SC based on LSTM model is depicted in Fig. 15. The following subsections describe in detailed each stage.

#### 6.1.1. Stage I - signal acquisition

The same fault current and voltage signatures acquired in Section 4.1.1 were utilized as the data basis for the fault location regression problem with the LSTM model. For enabling a fair comparison between the schemes, the same sampling frequency of 20 kHz was considered.

#### 6.1.2. Stage II - feature extraction

At this stage, the Stationary Wavelet Transform (SWT) is applied as a power signal processing tool which detects signal singularities and extracts the useful insights from voltages and currents measurements. SWT is a widely used Wavelet Transformation (WT) for different power system applications (i.e., protection applications), as it is computationally efficient and presents reduced complexity [5,45].

For the LSTM-based fault location scheme the faulted voltage and current signatures are subjected to level 1 and level 2 decomposition through the SWT technique, and the corresponding detail coefficients are produced, utilizing the *db4* mother wavelet. As the exhaustive research of the appropriate decomposition level and the type of mother wavelet is out of the scope of the presented research, a detailed analysis is reported by the authors in [5].

Once the detail coefficients of decomposition levels 1 and 2 are acquired, a moving data window with length of 30 samples (29-sample overlap), has been utilized. The principal objective of the window-based method is to disclose hidden information related to the nature and the evolution of fault and form the corresponding feature vectors. The production of the feature vectors is performed at the end of the stage II. In particular, from the absolute values of detail coefficients at both levels, the sum  $\Sigma(D_j)$ , the mean  $\mu(D_j)$ , the standard deviation  $\sigma(D_j)$  and the energy content  $E(D_j)$  are calculated according to the (12)–(15), respectively [5]:

$$\Sigma(D_j) = \sum_{i=1}^{m_w} |D_j(i)| \quad (12)$$

$$\mu(D_j) = \frac{1}{2^j \cdot m_w} \sum_{i=1}^{m_w} |D_j(i)| \quad (13)$$

$$\sigma(D_j) = \sqrt{\frac{1}{2^j \cdot m_j} \sum_{i=1}^{m_w} (|D_j(i)| - \mu(D_j))^2} \quad (14)$$

$$E(D_j) = \sum_{i=1}^{m_w} [D_j(i)]^2 \quad (15)$$

where  $D_j(i)$  denotes the  $i$ th detail coefficient for  $j = 1, 2$  decomposition level and  $m_w$  is equal to the window size.

At the data pre-processing stage, prior to the training of the LSTM model, the feature vectors along with the initial three phase current and voltage signatures are normalized. For the normalization process the mean value is subtracted by each sample in the feature vector and the resulting values is divided by the standard deviation as presented in (16):

$$Y_{j,scaled} = \frac{Y_j - \bar{Y}}{\sigma(Y)} \quad (16)$$

where  $Y_j$  denotes each sample in the feature vector  $y$  or current/voltage signal  $y$ ,  $\bar{Y}$  and  $\sigma(Y)$  correspond to the mean value and the standard deviation of each feature vector of current/voltage signal, respectively.

#### 6.1.3. Stage III - estimation of fault location

The normalized feature vectors and the normalized three phase current and voltage signatures have been reshaped into a three-dimensional matrix (batch size, sequence length, features), in order to meet the requirements of the LSTM input data and are used as inputs to train the LSTM model. Therefore, during the training process the LSTM input size is (32, 1600, 6). The output of the LSTM layer is fed into a fully connected layer followed by a regression layer which produced the single value of the fault position as percentage of the SC length, similarly to the CNN model.

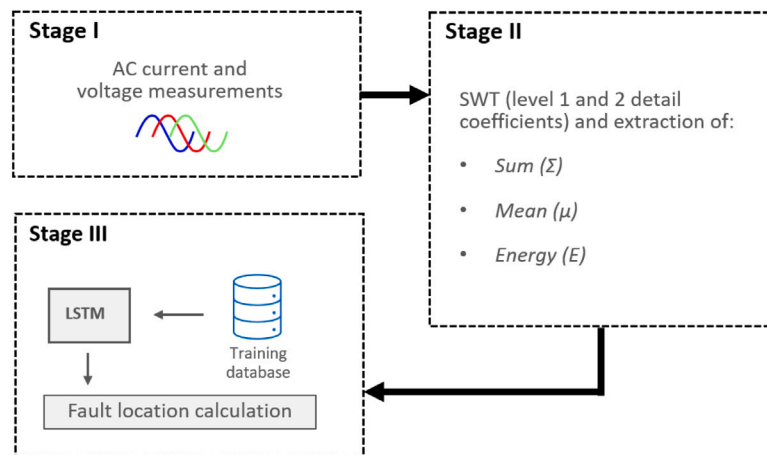


Fig. 15. Schematic diagram of the LSTM-based fault location schemes.

Table 10

Tested LSTM-based schemes and their performance on the testing dataset.

LSTM-based schemes	$\overline{error}_{FL}(\%)$
Scheme 1	0.95
Scheme 2	0.88

## 6.2. Selection of LSTM model

Two different LSTM-based schemes have been investigated considering different combinations of the algorithm stages presented in Fig. 15. The scope of this investigation was to evaluate the impact of different datasets on the LSTM fault location estimation capability and select the scheme with the best performance to be compared with the developed CNN-based scheme. For that reason two models have been developed: (i) the LSTM-based scheme 1 which contains the stages I and III, considering as inputs only the normalized three-phase current and voltage signatures, and (ii) the LSTM-based scheme 2 which includes the stages I, II and III, considering the inclusion of the SWT signal processing. The comparison between these two schemes evaluates the impact of the SWT technique at the pre-process stage on the fault location estimation accuracy.

The LSTM-based schemes have been developed utilizing the PyTorch framework. The most-suitable hyperparameters of each LSTM model and the best trained model have been selected based on the GS five-fold CV technique (similarly to the CNN model). Particularly, different combinations of (i) hidden state size, (ii) number of LSTM layers, (iii) learning rate and (iv) batch size have been tested utilizing the  $\overline{error}_{FL}$  as CV score given in (11).

The two LSTM-based schemes were evaluated on the testing dataset and the resulting  $\overline{error}_{FL}$  is presented in Table 10.

It is evident that the LSTM-based scheme 2 which incorporates the SWT technique, presents the lowest  $\overline{error}_{FL}$  and therefore, it has been selected for comparison purposes with the CNN-based fault location scheme. The resulting hyperparameters from the GS five-fold CV technique are the following: learning rate = 0.001, batch size = 32, hidden size = 64 and number of LSTM layers = 4. The Adam optimizer algorithm was adopted for learning the weights and biases associated with the model during the training process.

## 6.3. Results of the comparison between the LSTM and the CNN algorithm

This section presents the results of the comparative analysis between the proposed CNN-based fault location scheme and the LSTM-based scheme 2. Both algorithms have been evaluated for additional

Table 11

Results of the comparison between the CNN-based and LSTM-based fault location schemes.

Fault type	$R_f$ ( $\Omega$ )	$A.C_f$ (km)	CNN $error_{FL}(\%)$	LSTM $error_{FL}(\%)$
3-Ph-G	0	0.60	0.70	2.40
3-Ph-G	200	5.90	0.22	3.40
3-Ph-G	15	9.10	0.28	2.10
3-Ph-G	0	0.10	1.10	3.10
3-Ph-G	2	4.20	0.12	0.70
3-Ph-G	200	9.20	0.48	0.82
Ph-Ph-G	2	2.90	0.90	1.20
Ph-Ph-G	5	7.30	0.10	1.00
Ph-G	0	1.70	0.30	1.90
Ph-G	300	9.90	0.27	1.50

fault cases which simulated different fault types, varying fault position (which do not belong to the initial data set) and varying fault resistance. The  $\overline{error}_{FL}$  of the CNN-based model has been found to be 0.73%, while for the LSTM-based model 1.10%. The results of some representative cases are presented in Table 11. The obtained observations validate the effectiveness of the proposed fault location scheme, as the CNN model yields lower  $error_{FL}$  compared to the LSTM model for all the scenarios. The  $\overline{error}_{FL}$  of the CNN-based scheme for the presented scenarios in Table 11 is 0.47% and for the LSTM-based scheme 2 is 1.82%. It is evident that the CNN-based fault location scheme outperforms the LSTM algorithm and provides more accurate fault localization irrespective of the fault type, the fault resistance or fault position.

## 7. Conclusion

The presented work proposes a novel data-driven fault location scheme for power grids with SCs and presence of CIGs. Considering the quenching of the SCs and the limitations of the conventional fault location schemes, the AI-based techniques can provide a very promising solution for accurate fault location estimation on the SCs. The proposed fault location scheme relies on the captured fault current and voltage signatures from the single end of the SC and utilizes the combination of time to time-to-frequency transformation and CNN algorithm for the fault location estimation. Specifically, after an extensive investigation of CNN algorithms with regards to the resulting mean fault location estimation error,  $\overline{error}_{FL}$ , the Inception-v3 model has been selected for the image analysis of the constructed spectrograms.

The proposed scheme has been found to successfully provide accurate estimation of the fault location across a wide range of fault conditions, accounting for different fault positions, fault types, values of fault resistance and the fault inception angles. It is worth highlighting

that the developed fault location scheme presented robust performance even in the case of close-up faults (i.e., fault location at 2% or 99% of SC length). Furthermore, the proposed CNN-based algorithm provides accurate fault location estimation under the influence of highly-resistive faults during which there is no quenching of the SC. The fault location estimation error has been found to lie within the range of 0.009% to 1.20% with respect to the SC length. Additionally, the effectiveness of the proposed method has been verified against small increments of fault location and additive noise in the testing datasets. The increased generalization capability of the proposed scheme leads to the accurate fault location estimation and there is no need for perturbation techniques during the training process to mitigate the overfitting to the training dataset.

Finally, the reliability of the proposed fault location scheme has been demonstrated by comparing its performance with an LSTM-based network which is a widely-used algorithm for fault location applications. The results indicate that the proposed CNN-based scheme outperforms the LSTM-based scheme in terms of fault localization accuracy. Conclusively, the developed fault location scheme is accurate, reliable and can be considered a viable solution to resolve the fault location problem on the SCs.

### CRedit authorship contribution statement

**Eleni Tsotsopoulou:** Conceptualization, Methodology, Investigation, Formal analysis, Validation, Writing – original draft. **Xenofon Karagiannis:** Software, Methodology, Writing – review & editing. **Theofilos Papadopoulos:** Methodology, Investigation, Supervision, Writing – review & editing. **Andreas Chrysochos:** Methodology, Investigation, Supervision, Writing – review & editing. **Adam Dyško:** Supervision, Writing – review & editing. **Qiteng Hong:** Writing – review & editing. **Dimitrios Tzelepis:** Methodology, Supervision, Writing – review & editing.

### Declaration of competing interest

The authors declare that they have no known competing financial interests or personal relationships that could have appeared to influence the work reported in this paper.

### Data availability

Data will be made available on request.

### References

- [1] Liu Y, et al. Dynamic state estimation for power system control and protection. *IEEE Trans Power Syst* 2021;28(6):5909–21. <http://dx.doi.org/10.1109/TPWRS.2021.3079395>.
- [2] Ballarino A, et al. The BEST PATHS project on MguppercaseB2 superconducting cables for very high power transmission. *IEEE Trans Appl Supercond* 2016;26(3):1–6. <http://dx.doi.org/10.1109/TASC.2016.2545116>.
- [3] Xiang W, et al. DC fault study of a point-to-point HVDC system integrating offshore wind farm using high-temperature superconductor DC cables. *IEEE Trans Energy Convers* 2022;37(1):377–88. <http://dx.doi.org/10.1109/TEC.2021.3094308>.
- [4] Su R, et al. Numerical model of HTS cable and its electric-thermal properties. *IEEE Trans Appl Supercond* 2019;29(5):1–5. <http://dx.doi.org/10.1109/TASC.2019.2901874>.
- [5] Tsotsopoulou E, Karagiannis X, Papadopoulos P, Dyško A, Yazdani-Asrami M, Booth C, et al. Time-domain protection of superconducting cables based on artificial intelligence classifiers. *IEEE Access* 2022;10:10124–38. <http://dx.doi.org/10.1109/ACCESS.2022.3142534>.
- [6] Santos GG, Vieira JCM. Optimal placement of fault indicators to identify fault zones in distribution systems. *IEEE Trans Power Del* 2021;36(5):3282–5. <http://dx.doi.org/10.1109/TPWRD.2021.3101671>.
- [7] IEEE guide for determining fault location on ac transmission and distribution lines. In: *IEEE Std C37.114-2014 (Revision of IEEE Std C37.114-2004)*. 2015, p. 1–76.
- [8] Aboshady F, Thomas D, Sumner M. A new single end wideband impedance based fault location scheme for distribution systems. *Electr Power Syst Res* 2019;173:263–70. <http://dx.doi.org/10.1016/j.epsr.2019.04.034>.
- [9] Shu H, Liu X, Tian X. Single-ended fault location for hybrid feeders based on characteristic distribution of traveling wave along a line. *IEEE Trans Power Del* 2021;36(1):339–50. <http://dx.doi.org/10.1109/TPWRD.2020.2976691>.
- [10] Lopes FV, Dantas KM, Silva KM, Costa FB. Accurate two-terminal transmission line fault location using traveling waves. *IEEE Trans Power Del* 2018;33(2):873–80. <http://dx.doi.org/10.1109/TPWRD.2017.2711262>.
- [11] Gao C, Wang L, Mao J, Hu S, Zhang B, Yang S. Non-intrusive cable fault diagnosis based on inductive directional coupling. *IEEE Trans Power Del* 2019;34(4):1684–94. <http://dx.doi.org/10.1109/TPWRD.2019.2918173>.
- [12] Chang SJ, Park JB. Multiple Chirp reflectometry for determination of fault direction and localization in live branched network cables. *IEEE Trans Instrum Meas* 2017;66(10):2606–14. <http://dx.doi.org/10.1109/TIM.2017.2700178>.
- [13] Pignati M, Zanni L, Romano P, Cherkaoui R, Paolone M. Fault detection and faulted line identification in active distribution networks using synchrophasors-based real-time state estimation. *IEEE Trans Instr Meas* 2017;32(1):381–92. <http://dx.doi.org/10.1109/TPWRD.2016.2545923>.
- [14] Bountouris P, Guo H, Tzelepis D, Abdulhadi I, Coffele F, Booth C. MV faulted section location in distribution systems based on unsynchronized LV measurements. *Int J Electr Power Energy Syst* 2020;119:105882. <http://dx.doi.org/10.1016/j.ijepes.2020.105882>.
- [15] Jia K, Yang B, Bi T, Zheng L. An improved sparse-measurement-based fault location technology for distribution networks. *IEEE Trans Ind Inform* 2021;17(3):1712–20. <http://dx.doi.org/10.1109/TII.2020.2995997>.
- [16] Chen W, Wang D, Cheng D, Qiao F, Liu X, Hou M. Novel travelling wave fault location principle based on frequency modification algorithm. *Int J Electr Power Energy Syst* 2022;141:108155. <http://dx.doi.org/10.1016/j.ijepes.2022.108155>.
- [17] Xie L, Luo L, Ma J, Li Y, Zhang M, Zeng X, et al. A novel fault location method for hybrid lines based on traveling wave. *Int J Electr Power Energy Syst* 2022;141:108102. <http://dx.doi.org/10.1016/j.ijepes.2022.108102>.
- [18] Bang SS, Shin Y-J. Abnormality monitoring for three-phase HTS cable via time-frequency domain reflectometry. *IEEE Trans Appl Supercond* 2021;31(5):1–6.
- [19] Lee C-K, Kwon G-Y, Lee YH, Lee GS, Bang SS, Shin Y-J. Insulation characteristics and fault analysis of HTS cable via stepped frequency waveform reflectometry. *IEEE Trans Appl Supercond* 2019;29(5):1–5. <http://dx.doi.org/10.1109/TASC.2019.2903740>.
- [20] Lee GS, et al. Time-frequency-based insulation diagnostic technique of high-temperature superconducting cable systems. *IEEE Trans Appl Supercond* 2016;26(4):1–5. <http://dx.doi.org/10.1109/TASC.2016.2524520>.
- [21] Yang B, Tang J, Yang C, Dong X, Huang K, Feng C. High-temperature superconducting cable fault location method based on improved time-frequency domain reflection method and EEMD noise reduction. *Math Probl Eng* 2021;2021:1–10. <http://dx.doi.org/10.1155/2021/9590969>.
- [22] Guillen D, Salas C, Trillaud F, Castro LM, Queiroz AT, Sotelo GG. Impact of resistive superconducting fault current limiter and distributed generation on fault location in distribution networks. *Electr Power Syst Res* 2020;186:106419. <http://dx.doi.org/10.1016/j.epsr.2020.106419>.
- [23] Moradzadeh A, Teimourzadeh H, Mohammadi-Ivatloo B, Pourhossein K. Hybrid CNN-LSTM approaches for identification of type and locations of transmission line faults. *Int J Electr Power Energy Syst* 2022;135:107563. <http://dx.doi.org/10.1016/j.ijepes.2021.107563>.
- [24] Belagoune S, Bali N, Bakdi A, Baadji B, Atif K. Deep learning through LSTM classification and regression for transmission line fault detection, diagnosis and location in large-scale multi-machine power systems. *Measurement* 2021;177:0263–2241.
- [25] Gashteroodkhani O, Majidi M, Etezadi-Amoli M, Nematollahi A, Vahidi B. A hybrid SVM-TT transform-based method for fault location in hybrid transmission lines with underground cables. *Electr Power Syst Res* 2019;170:205–14.
- [26] Stefanidou-Voziki P, Cardoner-Valbuena D, Villafafila-Robles R, Dominguez-Garcia J. Data analysis and management for optimal application of an advanced ML-based fault location algorithm for low voltage grids. *Int J Electr Power Energy Syst* 2022;142:108303. <http://dx.doi.org/10.1016/j.ijepes.2022.108303>.
- [27] Rezaee Ravesh N, Ramezani N, Ahmadi I, Nouri H. A hybrid artificial neural network and wavelet packet transform approach for fault location in hybrid transmission lines. *Electr Power Syst Res* 2022;204:107721. <http://dx.doi.org/10.1016/j.epsr.2021.107721>.
- [28] Tavooji S, Shirkhani M, Azizi A, Ud Din S, Mohammadzadeh A, Mobayen S. A hybrid approach for fault location in power distributed networks: Impedance-based and machine learning technique. *Electr Power Syst Res* 2022;210:108073. <http://dx.doi.org/10.1016/j.epsr.2022.108073>.
- [29] Yazdani-Asrami M, Seyyedbarzegar S, Sadeghi A, de Sousa WTB, Kottonau D. High temperature superconducting cables and their performance against short circuit faults: current development, challenges, solutions, and future trends. *Supercond Sci Technol* 2022;35(8):083002. <http://dx.doi.org/10.1088/1361-6668/ac7ae2>.

- [30] Yu Y, Li M, Ji T, Wu QH. Fault location in distribution system using convolutional neural network based on domain transformation. *CSEE J Power Energy Syst* 2021;7(3):472–84. <http://dx.doi.org/10.17775/CSEEJPES.2020.01620>.
- [31] SuperPower. SuperPower 2G HTS wire specifications. 2013.
- [32] Hong Z, Campbell A, Combs T. Numerical solution of critical state in superconductivity by finite element software. *Supercond Sci Technol* 2006;19(12):1246–52. <http://dx.doi.org/10.1088/0953-2048/19/12/004>.
- [33] Bottura L. Cable stability. In: *CERN in the proceedings of the CAS-CERN accelerator school: superconductivity for accelerators, erice, italy, Vol. 2*. 2014.
- [34] Ametani A. A general formulation of impedance and admittance of cables. *IEEE Trans Power App Syst* 1980;PAS-99(3):902–10. <http://dx.doi.org/10.1109/TPAS.1980.319718>.
- [35] Gudmundsdottir US, Gustavsen B, Bak CL, Wiechowski W. Field test and simulation of a 400-kV cross-bonded cable system. *IEEE Trans Power Del* 2011;26(3):1403–10. <http://dx.doi.org/10.1109/TPWRD.2010.2084600>.
- [36] Welch P. The use of fast Fourier transform for the estimation of power spectra: A method based on time averaging over short, modified periodograms. *IEEE Trans Audio Electroacoust* 1967;15(2):70–3. <http://dx.doi.org/10.1109/TAU.1967.1161901>.
- [37] Wang D, Yang D, Bowen Z, Ma M, Zhang H. Transmission line fault diagnosis based on wavelet packet analysis and convolutional neural network. In: *2018 5th IEEE international conference on cloud computing and intelligence systems*. 2018, p. 425–9. <http://dx.doi.org/10.1109/CCIS.2018.8691304>.
- [38] Sharma N, Jain V, Mishra A. An analysis of convolutional neural networks for image classification. *Procedia Comput Sci* 2018;132:377–84. <http://dx.doi.org/10.1016/j.procs.2018.05.198>.
- [39] Herlender J, Izykowski J, Solak K. Compensation of the current transformer saturation effects for transmission line fault location with impedance-differential relay. *Electr Power Syst Res* 2020;182:106223. <http://dx.doi.org/10.1016/j.epsr.2020.106223>.
- [40] Naseri F, Kazemi Z, Farjah E, Ghanbari T. Fast detection and compensation of current transformer saturation using extended Kalman filter. *IEEE Trans Power Del* 2019;34(3):1087–97. <http://dx.doi.org/10.1109/TPWRD.2019.2895802>.
- [41] Tzelepis D, et al. Voltage and current measuring technologies for high voltage direct current supergrids: A technology review identifying the options for protection, fault location and automation applications. *IEEE Access* 2020;8:203398–428. <http://dx.doi.org/10.1109/ACCESS.2020.3035905>.
- [42] Feng X, Pei W, Jia Z, Chen F, Zhang D, Lu G. Deep-masking generative network: A unified framework for background restoration from superimposed images. *IEEE Trans Imag Process* 2021;30:4867–82. <http://dx.doi.org/10.1109/TIP.2021.3076589>.
- [43] He K, Gkioxari G, Dollar P, Girshick R. Mask R-CNN. In: *Proceedings of the IEEE international conference on computer vision*. ICCV, 2017, <http://dx.doi.org/10.1109/ICCV.2017.322>.
- [44] Belagoune S, Bali N, Bakdi A, Baadji B, Atif K. Deep learning through LSTM classification and regression for transmission line fault detection, diagnosis and location in large-scale multi-machine power systems. *Measurement* 2021;177:109330. <http://dx.doi.org/10.1016/j.measurement.2021.109330>.
- [45] Tzelepis D, Fusiek G, Dyško A, Niewczas P, Booth C, Dong X. Novel fault location in MTDC grids with non-homogeneous transmission lines utilizing distributed current sensing technology. *IEEE Trans Smart Grid* 2018;9(5):5432–43. <http://dx.doi.org/10.1109/TSG.2017.2764025>.